INVESTIGATION OF VORTEX-INDUCED VIBRATIONS TO COMPARE REYNOLDS-AVERAGE NAVIER-STOKES AND DETACHED-EDDY SIMULATIONS

Kilian M. Streitenberger[1] and Jens Nitzsche[1]

[1]Institute of Aeroelasticity, German Aerospace Center (DLR), 37073 Göttingen
kilian.streitenberger@dlr.de

Keywords: vortex-induced vibrations, limit-cycle oscillations, lock-in, detached-eddy simulation

Abstract: We investigate vortex-induced vibrations (VIV) of a vertically spring-suspended NACA0021 airfoil at very high angles of attack of 60° and 70° at a chord Reynolds number of 2.7×10^5 by comparison of two-dimensional Reynolds-averaged Navier-Stokes (RANS) and three-dimensional delayed detached-eddy (DDES) simulations. For the non-moving airfoil, the simulated flow field is already highly unsteady due to pronounced wake vortex shedding with a dominant Strouhal number of $Sr \approx 0.19$ and with large qualitative differences in the spectral content of RANS and DDES integral forces. These differences decrease significantly when the airfoil is conducting sine-like motions either by prescribed forcing or via free fluid-structure interaction. No major differences occur between RANS and DDES in the resulting maximum VIV limit-cycle amplitudes under lock-in conditions, while the lock-in frequency range is slightly narrower for DDES. During lock-in a remarkable reduction in the turbulent intensity can be observed in the scale-resolving simulations.

1 INTRODUCTION

The continuous growth in available computing power is increasingly enabling the use of scale-resolving CFD methods for aeroelastic problems. The expectations associated with this are twofold: On the one hand, progress in turbulence modeling itself, i.e. the de facto replacement of previous, often still inadequate eddy viscosity or Reynolds stress models and thus improved modeling of the time-mean or unsteady ensemble average of detached off-design flows. On the other hand, scale-resolving methods enable the representation of small turbulent scales in the first place and thus the modeling of potential "turbulence-structure interaction" problems, the latter under the limitation of the natural low-pass behavior of solid structures due to inertia, i.e. the solid structures in such scenarios would have to be small enough to be receptive to the then comparatively large turbulent flow features.

In this study we investigate so called vortex-induced vibrations (VIV) [1] as a promising candidate for an interaction, where the dominant frequencies of the resolved turbulence may be low enough to interact with an underlying elastic structure and hence a considerable difference between RANS and DES could be expected. VIV refers to one-degree-of-freedom limit-cycle flutter of a bluff body cylinder in heavily separated flow that exhibits itself a dominant natural frequency due to periodic Van-Karmán type vortex shedding. The maximum flow-induced vibration amplitudes usually occur when the structural eigenfrequency is sufficiently close to the vortex shedding frequency and nonlinear synchronisation, the so called lock-in can be observed. Our main focus is on the difference between RANS and DES based fluid-structure

coupled simulation with respect to the frequency and amplitude of the resulting flow-induced vibrations.

1.1 Literature overview

There are some previous investigations which compare RANS and scale-resolving CFD for aeroelastic problems like Im et al. [2], Patel et al. [3] and Sun et al. [4]. They did DES simulations for turbo machinery, especially Sun did a stability analysis for a last-stage steam turbine blade. Compared to RANS the DES simulation shows an influence to the local damping at the blade tip due to the gap, which courses a tip leakage vortex, while the global flutter behavior of the blade was not affected. Wang and Zha [5] compared RANS and DES results for transonic limit-cycle oscillations with a fully coupled fluid-structure-interaction (FSI) simulation. They also show marginal differences in the flow field with no influence to the flutter behavior.

With regard to VIV, numerous investigations were carried out on circular cylinders. Williamson and Roshko analysed an experiment for a cylinder, which is forced to sinusoidal motion in the vertical direction [6]. They identified different aerodynamic modes in the lock-in regime, depending on amplitude and frequency that affect the aerodynamic damping. Nguyen and Nguyen [7] compared RANS and DES with an experiment of Norberg [8] for a fixed circular cylinder. The DES simulation shows a better agreement in terms of the average forces to the experimental data than RANS. They also analysed the influence of the height of this cylinder on the root mean square (RMS) of the crossflow force. The higher the ratio of diameter to height, the smaller the RMS value. The frequency of the vortices is not influenced by this and shows approximately the same value for RANS, DES and the experiment. For the vibrating circular cylinder with one and two degrees of freedom, they only did FSI simulations with DES. The results are in good agreement to experiments of Hover et al. [9] and Williamson and Govardhan [1].

Vortex-induced vibrations are a field of growing interest in the design of horizontal-axis wind turbines. Especially when the rotor is stationary very high angles of attack (AoA) can occur locally at the blades. This can cause periodic vortex shedding with potential vortex-induced vibrations [10–13]. In this context Benner et al. [14] demonstrated vortex-induced vibrations on a NACA0021 airfoil for high AoAs up to 90° in a water tunnel experiment at low Reynolds numbers. Beginning at 60° AoA, the airfoil shows crossflow vibrations with small amplitudes for reduced frequencies between 0.938 and 1.083. With higher AoAs the amplitude and the frequency regime of lock-in increases. Grindersley et al. [15] performed a numerical sensitivity study on a 3-d wind turbine blade for different turbulence models, including RANS and DES. They used a forced-motion approach to compute the aerodynamic power acting on the first structural eigenmode. It was found that, compared to DES, RANS yields a higher coherence in spanwise direction. Depending on the flow cases this causes some differences, which results in higher VIV amplitudes for RANS.

1.2 Testcase

To compare RANS and DES a basic testcase has to be defined. In the project DESider [16] such a case was investigated for a stationary NACA0021 with 60° AoA at Mach 0.1 and a Reynolds number of 2.7×10^5. They focus on different background RANS-Models of the DES approach, the influence of the span and grid refinement. The results show a large vortex-street like behavior behind the airfoil with a discrete peak in the power spectrum. This suggests that elastic suspension may lead to VIV and lock-in. Based on this we use the same flow conditions and the same extruded airfoil with a span of two times the chord to resolve the
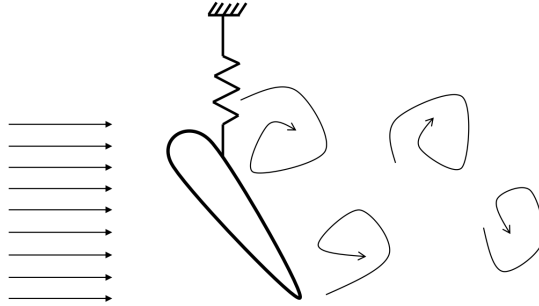
Figure 1: Schematic testcase setup

spanwise components of the turbulence. Additionally, the airfoil is allowed to move in cross-flow direction. For the RANS simulations we only use a two-dimensional airfoil. Figure 1 shows the schematic testcase setup. We investigate VIV at two different AoAs, first at 60° and later at 70° to see a larger lock-in regime. For the structural part we set the mass per meter in spanwise direction to 1 kg/m, resulting to a mass ratio of approximately 50. The stiffness is variable, so we can manipulate the natural frequency in vacuum of the system. Structural damping is not considered.

2 NUMERICAL SETUP

For computational analysis the DLR-Tau-Code is used. This unstructured-grid CFD-solver is able to solve the unsteady RANS equations as well as the modified Navier-Stokes equations for DES with different background turbulence models. DES is a hybrid RANS-LES approach, which was first published by Spalart et al. in 1997 to reduce the computational cost of scale-resolving CFD [17]. The idea is to use RANS instead of LES in the boundary layer, where a high grid resolution would be required for LES. In the other regions of the flow field the LES is used to resolve the small-scale turbulence. To switch between RANS and LES, a so-called DES-limiter is implemented. For the classic DES this limiter depends on the grid-spacing and the distance to the wall. If the grid spacing in the boundary layer is very small, the limiter switches to LES in the boundary layer. This can cause a grid-induced separation (GIS). To prevent this, an additional parameter was added to the limiter. The additional constraint depends on the eddy viscosity, a variable of the solution itself. This approach is called delayed detached eddy simulation (DDES) [18]. For the DES simulations in this paper we are using DDES.

2.1 DDES setup

For grid generation, DES requires some specific aspects, which are listed in [19]. In this report the grid is separated in different regions to take the different turbulence models of this hybrid RANS-LES approach into account.

This scheme was used to create five different unstructured grids, with up to 18.5 million grid points for the 60° AoA case. Figure 2 shows the medium grid with 5.3 million grid-points. The span is two times the chord to resolve the three-dimensional turbulence. Table 1 shows the parameters of these grids. The timestep size Δt depends on the grid-spacing in the focus-region behind the airfoil Δ_0 and the maximum estimated local velocity U_{max}. It can be calculated with

$$\Delta t = \frac{\Delta_0}{U_{max}} \tag{1}$$

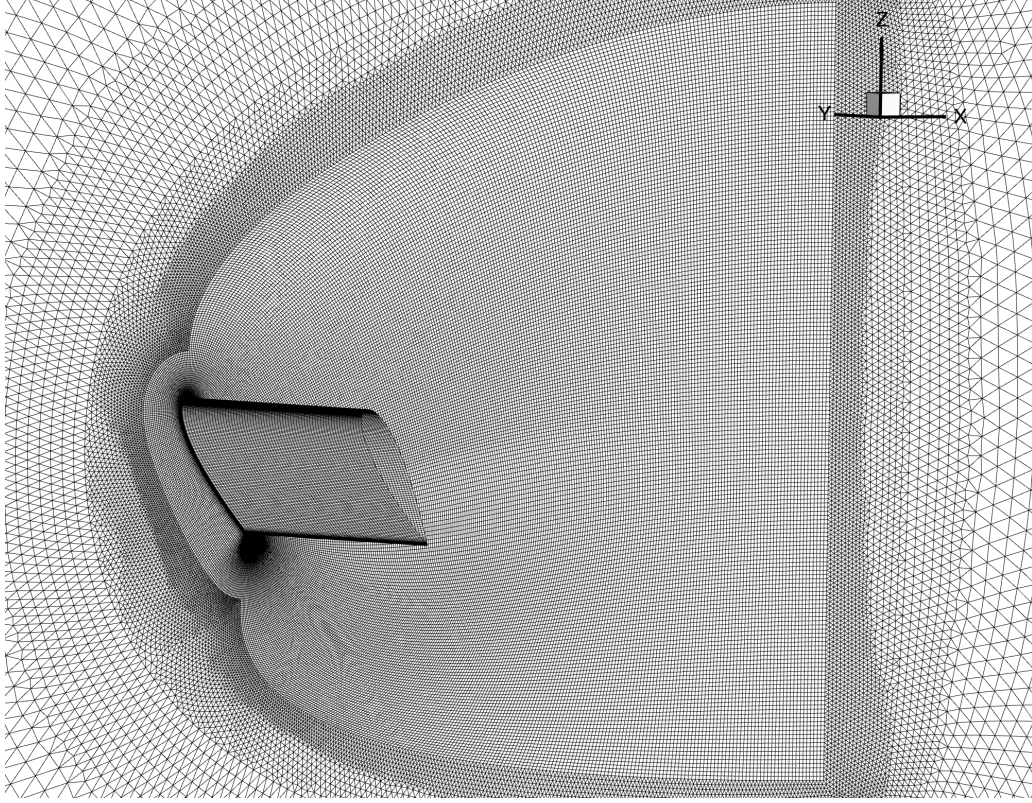[19]. From some previous simulations we estimated the maximum local velocity to 1.7 times

Figure 2: DDES medium grid

the incoming velocity. With

$$t^* = t \cdot U_\infty / c \tag{2}$$

we get a non-dimensional timestep size for every grid. To analyse and compare the mean integral forces of all grids, the solution must converge statistically. To reach this convergence, we need a minimum of $300 - 400$ convective time units [16]. Figure 3 shows the development of the mean lift coefficient (C-lift) over time. The very-fine grid simulation was cancelled after 14 days reaching around 300 convective time units. When we look at the other grids, we see a great improvement from coarse to medium compared to the experimental data of Swalwell et al. [20]. For the dual-time stepping scheme a convergence control for is used inside one physical timestep. For further simulations we used the medium grid, it is a good compromise between accuracy and computing time. For the 70° AoA case we use the same grid resolution, without doing an extra study of grid refinement.

Table 1: Comparison of the different DDES-grids

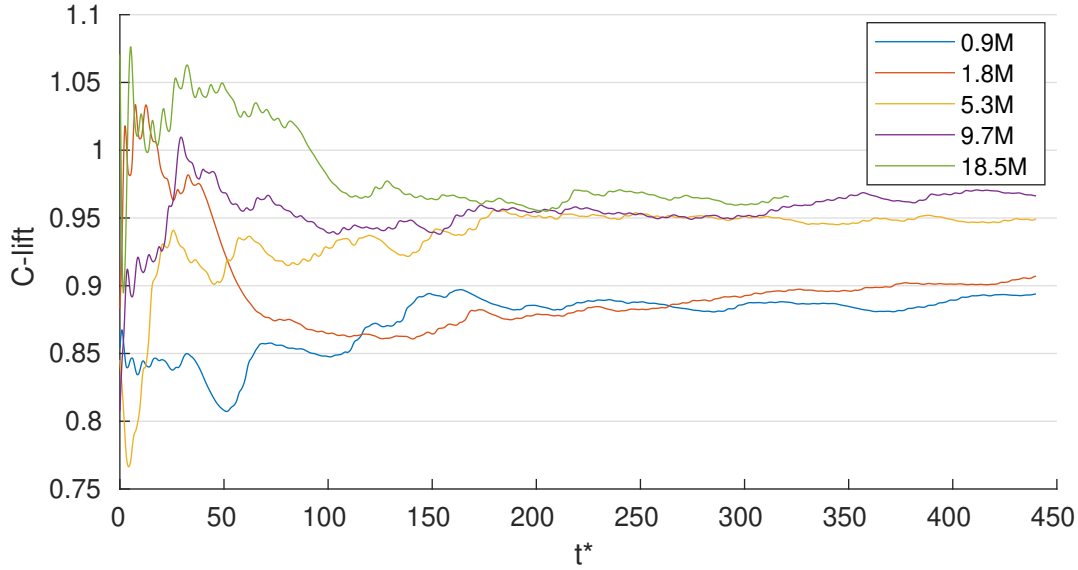|	very coarse	coarse	medium	fine	very fine	experimental data [20]
total number of points	0.9 M	1.8 M	5.3 M	9.7 M	18.5 M	
points in scope	180	225	337	430	552	
spanwise points	31	45	67	81	103	
grid-spacing Δ_0	≈ 0.065	≈ 0.044	≈ 0.030	≈ 0.025	≈ 0.019	
timestep size Δt^*	3.73 %	2.59 %	1.75 %	1.40 %	1.11 %	
mean C-lift	0.894	0.907	0.949	0.966	0.966	0.931
mean C-drag	1.437	1.469	1.545	1.581	1.585	1.517

Figure 3: Development of the mean lift coefficient over time for different grids

2.2 RANS setup

The two-dimensional RANS grid is derived from the three-dimensional medium DES grid. Refinement and coarsening of the RANS grid only slightly change the integral forces acting on the airfoil. The non-dimensional unsteady timestep is $2\,\%$. A halving of the timestep size results in a change of the fourth decimal of the mean lift coefficient. For the RANS simulation we also use a convergence control to improve computing time. The turbulence closure we are using is the one-equation Spalart-Allmaras model.

2.3 Methods to compute structural dynamics

There are two common methods to investigate VIV. First, a fluid-structure interaction (FSI) simulation, with a direct time domain coupling, and second the forced-motion approach. We use both methods to investigate their suitability for scale-resolving CFD.

2.3.1 Fluid-structure interaction

For the FSI approach an implicit Newmark-scheme is used to solve the differential equation for the rigid body motion [21, 22].

$$M\ddot{u}(t) + Ku(t) = f(\dot{u}, u, t) \tag{3}$$

M is the mass, K the stiffness and u the displacement. Damping is not considered on the left-hand side. On the right-hand side, the aerodynamic forces acting on the airfoil are calculated
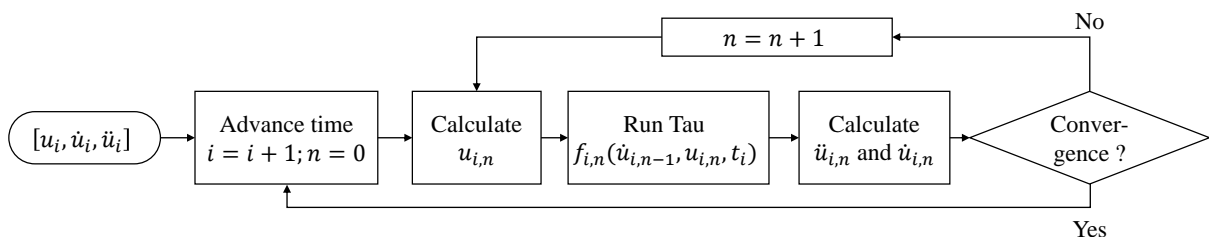

Figure 4: FSI Flowchart

5

by the CFD solver. The motion is updated every cycle, this results in a strong coupling with a fast convergence. To improve computational time, a Cauchy-like convergence control was implemented, so the same convergence criteria for the non-moving and the moving airfoil can be used. Figure 4 shows the flowchart of the FSI simulation.

2.3.2 Forced Motion

For simulations with the forced-motion approach, the motion is sinusoidal with a predefined normalised amplitude

$$H^* = \frac{H}{c} \tag{4}$$

with H representing the amplitude and c the chord length. The reduced frequency is defined by

$$\omega^* = Sr \cdot 2\pi = \frac{\omega \cdot c}{U_\infty} \tag{5}$$

where ω is the natural frequency and U_∞ the freestream velocity. To calculate the behavior of the real system we use and modify the approach of Morse and Williamson [23]. By dividing the aerodynamic forces F_{aero} in real and imaginary part, we get an aerodynamic damping and an additional effective mass, which can be normalised with the mass of the airfoil. They are defined by

$$c_{aero} = -\frac{\Im\left(F_{aero}(H^*, \omega^*)\right)}{H^* \cdot \omega^* \cdot U_\infty \cdot M} \tag{6}$$

and

$$m_{aero} = \frac{\Re\left(F_{aero}(H^*, \omega^*)\right)}{H^* \cdot (\omega^* \cdot U_\infty)^2 \cdot M} \tag{7}$$

and can be added to the equation of motion.

$$M\left(1 + m_{aero}\right)\ddot{u}(t) + Mc_{aero}\dot{u}(t) + Ku(t) = 0 \tag{8}$$

With a harmonic approach $u(t) = H^* \cdot e^{j\omega t}$, we get the eigenvalue problem

$$[K + j\omega Mc_{aero} - \omega^2 M(1 + m_{aero})]H^* = 0 \tag{9}$$

To solve this, we need to simulate a set of different amplitudes and frequencies. For this set, we can solve the imaginary part of equation 9. Because the aerodynamic damping is a function of the frequency and amplitude we can find their zero for every frequency

$$c_{aero}(H^*, \omega^*) = 0 \tag{10}$$

and get a correlated amplitude for vortex-induced vibrations.

$$H^*_{VIV} = f(\omega^*) \tag{11}$$

To calculate the stiffness and the reduced natural frequency in vacuum ω_0^*, we solve the real part of equation 9 for every frequency and their amplitude. This results in the following expression.

$$\omega_0^* = \omega^* \sqrt{1 + m_{aero}\left(H^*_{VIV}, \omega^*\right)} \tag{12}$$

This approach is more complex in post-processing than FSI simulations, but the same set of simulations can be used for different mass configurations. You can also get data outside the stable amplitude and investigate the influence of the frequency at these points. In contrast to the FSI simulation, the results of the forced-motion approach are not affected by an initial displacement. It's also possible to take damping into account without big changes.

6

3 RESULTS

3.1 Non-moving airfoil at 60° incident

The non-moving NACA0021 is a good configuration to show the characteristics of DDES compared to RANS. Figure 5 and 6 show the differences between these two methods. Especially in the power-spectral density (PSD) the resolved turbulence can be identified. The vortex-frequency of the scale-resolved simulation is slightly higher than in RANS, but in both we can see peaks at first and second harmonics. The higher harmonics in the DDES results cannot be identified, because of the turbulent noise. Looking at the time history plot in figure 6, the lift and drag of the scale-resolving simulation show a random-like behavior. This leads to high computational costs, because many time steps are needed for a converged mean value. Compared to DDES the RANS simulation shows a strong periodic behavior with a good convergence at low computational costs. The mean value of the integral forces for DDES are close to the experimental data of Swalwell et al. [20] and in the range of the different simulations done in the DESider project [16]. The RANS simulation leads to significantly higher values.
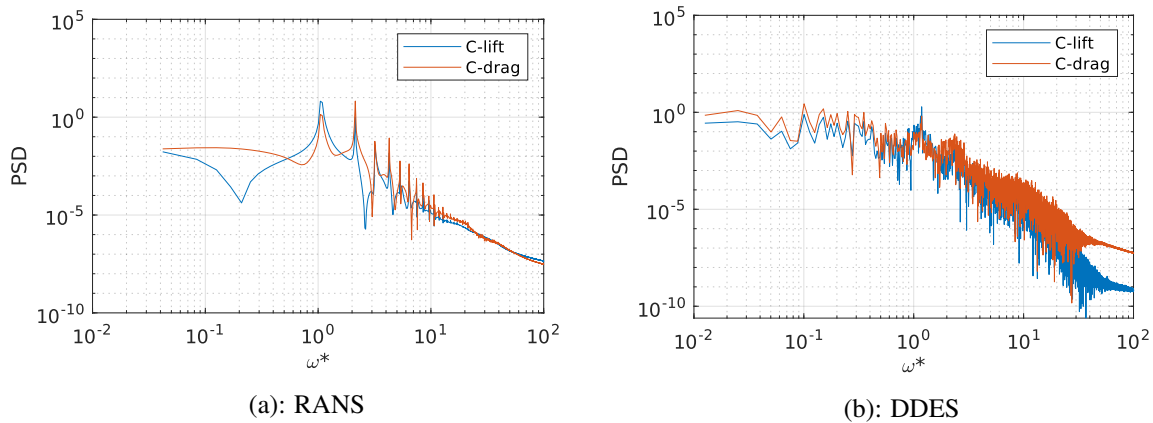

(a): RANS

(b): DDES

Figure 5: Comparison of lift and drag for RANS and DDES in frequency domain
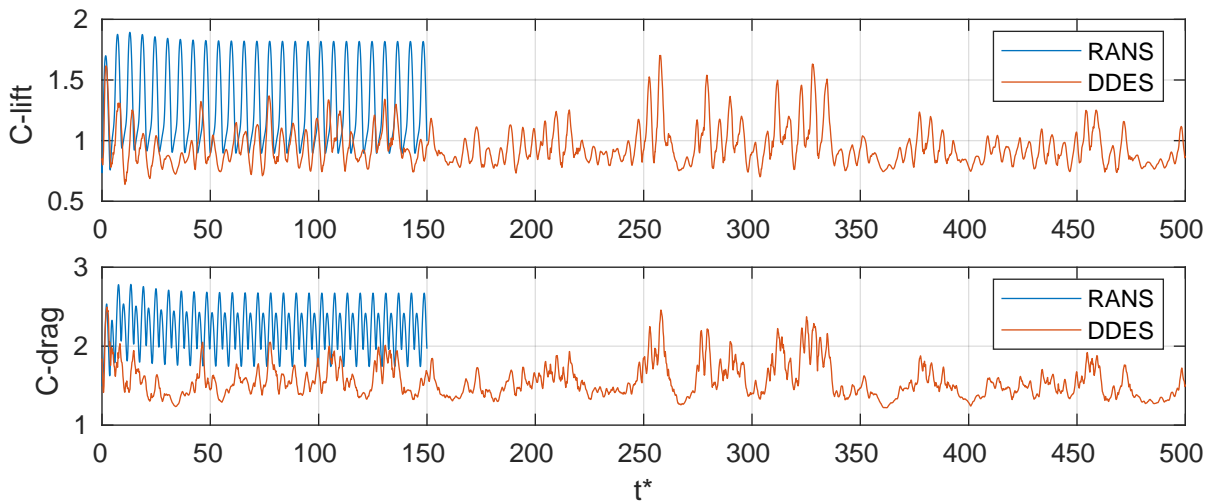

Figure 6: Comparison of lift and drag for RANS and DDES in time domain

7

3.2 Moving airfoil at 60° incident

To investigate the influence of the resolved turbulence on VIV, we compare simulations for different frequencies and AoAs using RANS and DDES. At 60° AoA we do some FSI simulations to identify the frequency range of lock-in. We already know from Benner et al. [14] that VIV just starts at this incident and gets more intensive at higher AoAs. For the RANS simulations we can detect a lock-in regime for reduced structural frequencies between 0.9 and 1.1. In this region we see a typical limit-cycle oscillation (LCO) behavior, as plotted in figure 7. It is noticeable that the mean lift coefficient drops to the the level of the DDES simulations as the amplitude increases. This effect is the same for every structural frequency inside the lock-in regime. Compared to RANS, the FSI simulation via DDES does not show LCOs for 60° AoA. In figure 8 the dynamic behavior of the coupled DDES simulation is plotted. To detect the synchronisation of the movement and the aerodynamic forces, the phase-shift between these two is added. Between $t^* = 130$ and $t^* = 200$ we can find a period of time, where lift and movement are synchronised and the amplitude increases. After this period, they begin to asynchronies again and the amplitude decreases. The fact, that lock-in in these conditions with
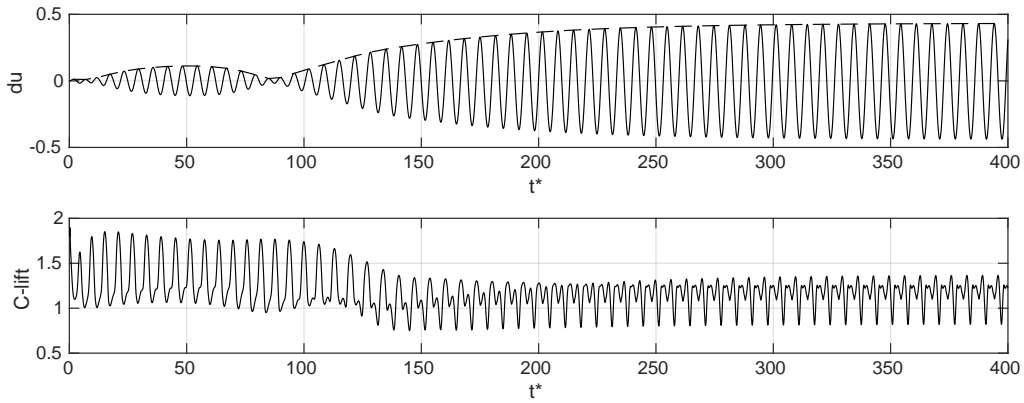

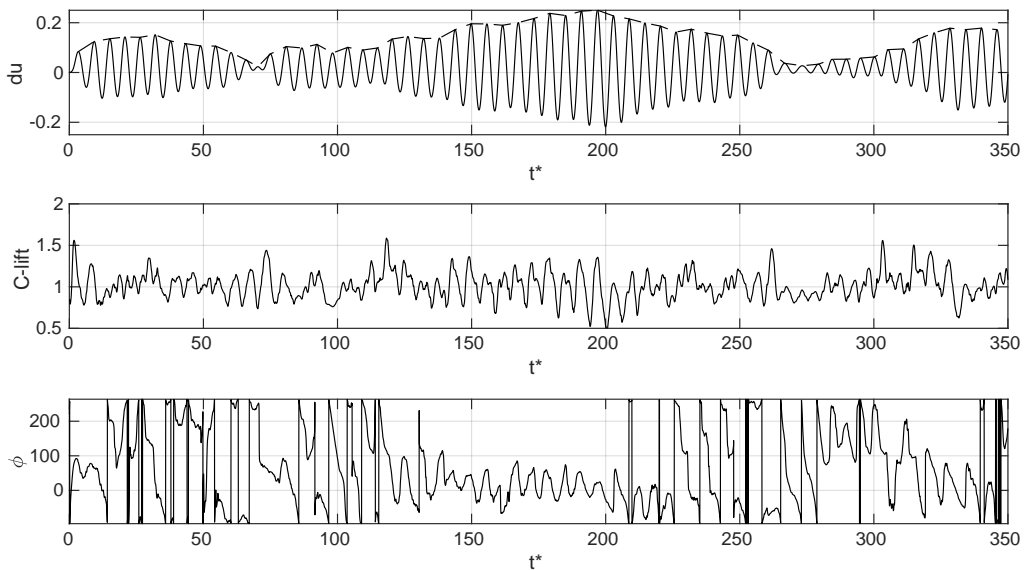Figure 7: LCO of the RANS-simulation at $\omega_0^* = 0.95$

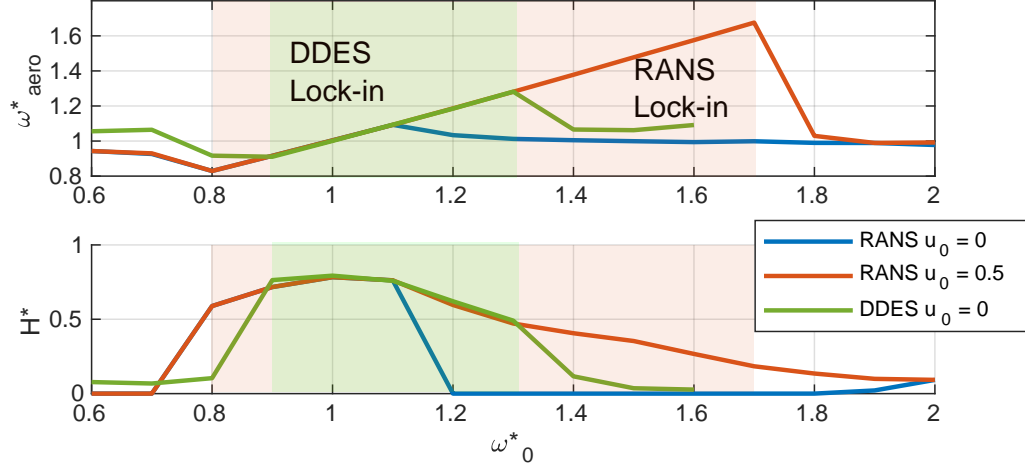Figure 8: time history plot of the DDES-simulation at $\omega_0^* = 1$

8

Figure 9: Comparison of frequency and amplitude of the FSI simulation for 70° AoA

DDES is only temporary, makes it complicate to analyse VIV. This implies that the maximum amplitude in the period under consideration may not be the maximum that could be physically reached. In addition, analysis in the frequency domain do not work for this case. Computing this behavior with the forced-motion approach does not work for DDES in this case, because the motion cannot be approximated with a sine and the resulting aerodynamic work is always negative.

3.3 Moving airfoil at 70° incident

For further investigations and to consider the interaction of motion and small-scale turbulence, we increase the AoA to 70°. Like before we start with FSI simulations to limit the range of frequencies for VIV. For this configuration LCOs occur for RANS and DDES. Figure 9 shows the first harmonics frequency for the aerodynamic forces plotted over the structural frequency in vacuum. When the ratio of both is near one, lock-in is detected. This affects a higher amplitude, which is shown below. The two different lines for RANS have two different initial displacements, this leads to a wider lock-in range for $u_0 = 0.5$. For DDES, different initial displacements do not change the lock-in regime. The range of VIVs frequencies is smaller for DDES than for RANS, because the RANS simulation tends to a premature vortex synchronisation. Comparing the maximum amplitude, there is no significant variance between RANS and the scale-resolving method.

To investigate the interaction of the motion and the resolved turbulence, we run forced-motion simulations for the 70° case. Furthermore, the objective is to demonstrate the ability of this approach to compute VIV with scale-resolving CFD. Therefor we do RANS simulations for a set of frequencies and amplitudes between $0.6 \leq \omega^* \leq 2.0$ and $0.1 \leq H^* \leq 0.9$. For DDES, the range of interest for the frequencies is slightly smaller, because of the tighter lock-in regime. This also saves computational costs. Figure 10(a) and (b) show the resulting aerodynamic damping of the forced-motion simulations, as well as the calculated VIV amplitude. There we can also see a wider range for the RANS simulation, where VIV occurs, but the maximum VIV amplitude is nearly the same. For the additional effective mass in figure 10(c) and (d), we also see no significant differences between RANS and DDES. Especially when comparing the ratio of the resulting structural frequency in vacuum and the VIV frequency via equation 12. On the left side of figure 11 these ratios for the forced-motion results and for the FSI simulations are plotted. Next to this plot, a comparison of the VIV amplitude is shown. There we
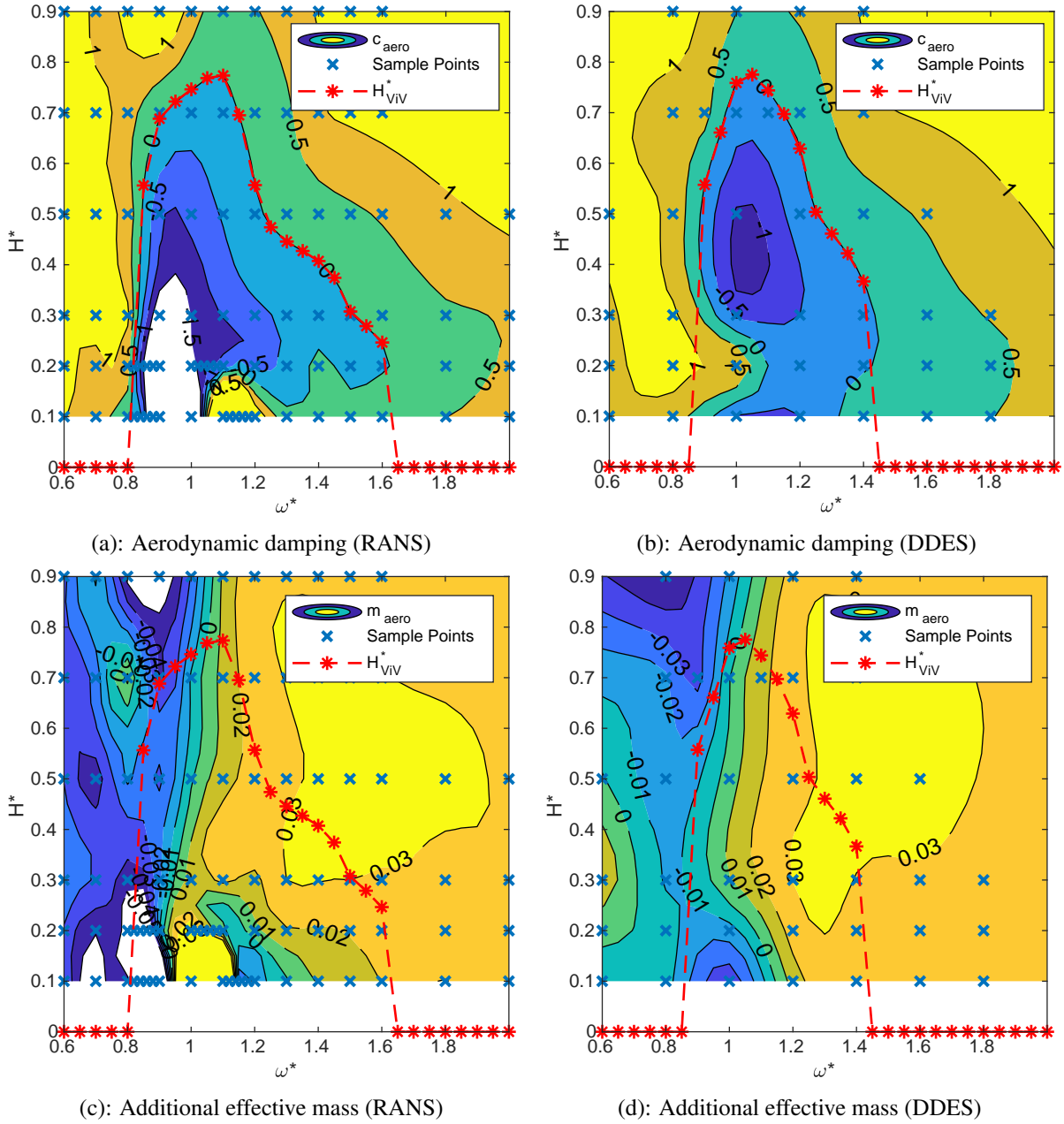
(a): Aerodynamic damping (RANS)

(b): Aerodynamic damping (DDES)

(c): Additional effective mass (RANS)

(d): Additional effective mass (DDES)

Figure 10: Comparison of the forced-motion results

(a): Ratio of structural and VIV frequency

(b): VIV amplitude
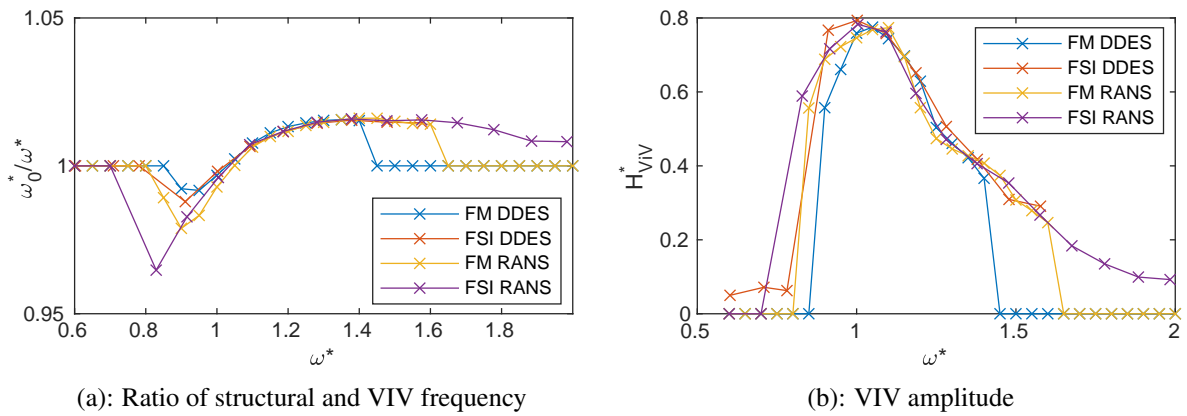
Figure 11: Comparison of forced-motion (FM) and FSI for DDES and RANS

(a): No lock-in at $\omega^* = 0.6$ and $H^* = 0.5$

(b): Lock-in at $\omega^* = 1.0$ and $H^* = 0.5$

(c): Lock-in at $\omega^* = 1.4$ and $H^* = 0.5$

(d): No lock-in at $\omega^* = 0.6$ and $H^* = 0.5$

(e): Lock-in at $\omega^* = 1.0$ and $H^* = 0.5$
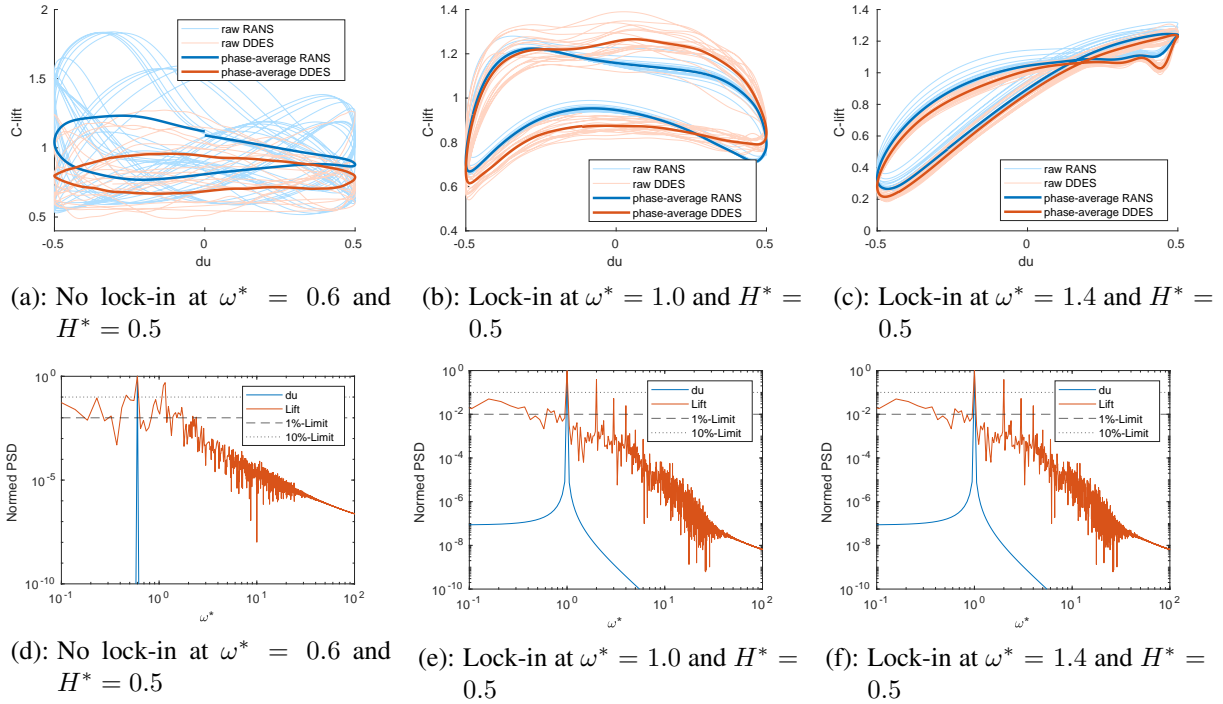
(f): Lock-in at $\omega^* = 1.4$ and $H^* = 0.5$

Figure 12: Top: Lissajous plots and below: PSD of the DDES simulations, normalized with the maximum value

also cannot see any significant differences between all four plots. This demonstrates that the forced-motion approach is an effective methodology for RANS and DDES.

In addition to the amplitude and frequency, we have a closer look at the data of the single forced-motion simulations done with DDES. In figure 12 we see some Lissajous plots and the normalized PSD. These plots are often used to detect lock-in. One advantage of the forced-motion approach is, that we can easily compute a phase-averaged lift coefficient for different amplitudes and frequencies. Comparing these phase-average curves we see a big difference between RANS and DDES outside of lock-in. With an increasing frequency inside the lock-in regime, they fit quite well. In addition to the Lissajous curves, we plotted the PSD of the Lift, normalized with the maximum peak, below. There we can see two horizontal lines. The 10% and the 1% line. Iyer [13] used these limits to detect lock-in. When the highest peak outside the harmonics is greater than the 10%-limit there is no lock-in. If it is smaller than the 1%-limit, lock-in occurs. In between a grey area exists. For higher frequencies this formulation of lock-in come to its limits, because the motion induced velocity and the resulting change of the AoA
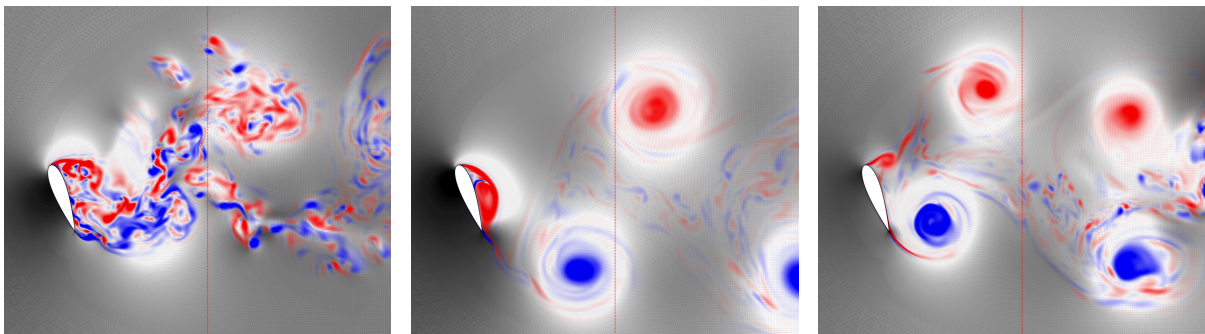
(a): No lock-in at $\omega^* = 0.6$

(b): Lock-in at $\omega^* = 1.0$

(c): Lock-in at $\omega^* = 1.4$

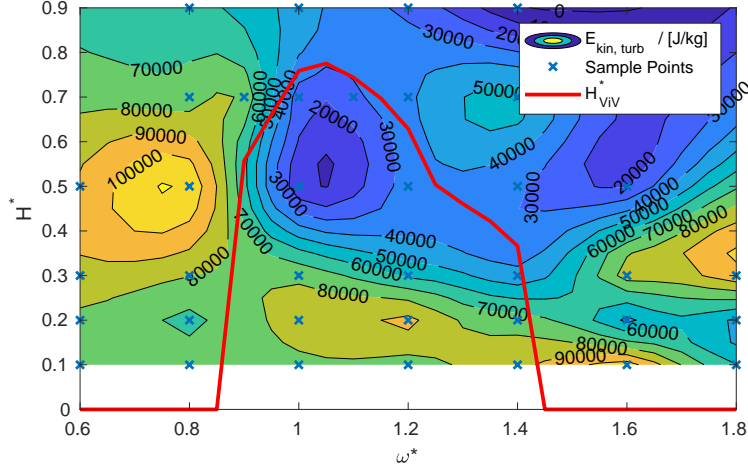Figure 13: DDES flow at $H^* = 0.5$; red line at $x = 2.25c$

11

Figure 14: Turbulent kinetic energy in the wake of the DDES flow

dominates the aerodynamic forces.

To understand the influence of the motion to the turbulent flow, we have a close look at figure 13. There we see the flow computed by DDES inside and outside of the lock-in regime. Remarkably, the intensity of the turbulent fluctuations is significantly smaller, when lock-in occurs. The flow resembles a typical RANS simulation. To quantify this, we analyse the mean turbulent kinetic energy in the cut plane marked in red for the last two periods. In figure 14 we can see a great impact of the movement to the turbulent kinetic energy in the range of amplitude and frequency, where VIV occur. Outside, the maximum turbulent kinetic energy is approximate ten times higher than the minimum inside. This shows that moving structural parts can affect turbulent flow in an astonishing manner. We also investigate the spanwise correlation in this cut plane. In figure 15 we can see a spanwise synchronisation during lock-in. For an easier comparison we introduce a coefficient for the overall spanwise correlation, which is defined by

$$R_V = \frac{\iint R(y,z) \cdot dydz}{\iint 1 \cdot dydz} \tag{13}$$

and represents the volume under the surfaces. This new correlation coefficient is plotted for the whole set of amplitudes and frequencies in figure 16. There we see a similar trend as shown in figure 14 for the turbulent kinetic energy. This means that lock-in do not only synchronise the large-scale vertices, it also smooths the small-scale turbulence.
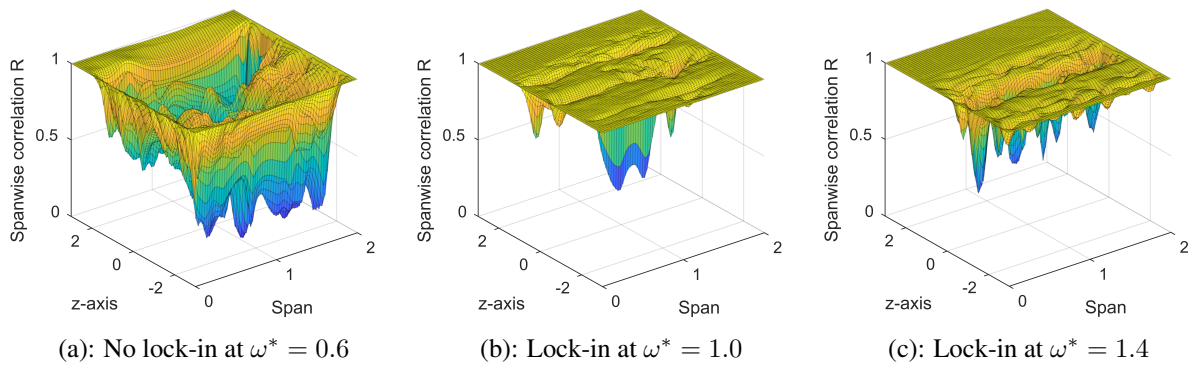

(a): No lock-in at $\omega^* = 0.6$ (b): Lock-in at $\omega^* = 1.0$ (c): Lock-in at $\omega^* = 1.4$

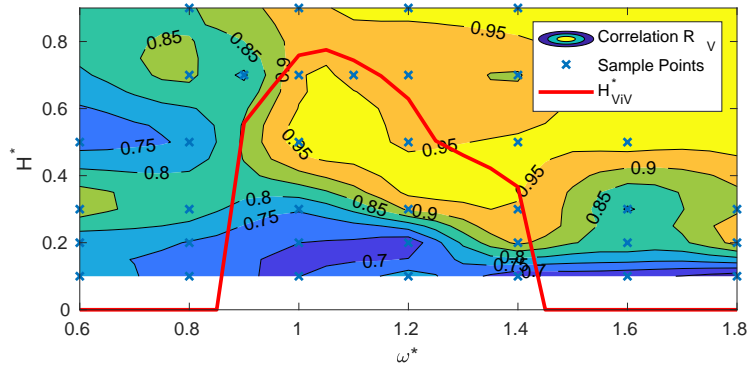Figure 15: Spanwise correlation for $H^* = 0.5$ at $x = 2.25c$

12

Figure 16: Spanwise correlation for the whole set of frequencies and amplitudes

4 CONCLUSION

There are some major key findings. We can divide them into fluid to structure and structure to fluid. First, we look at the fluid to structure findings. If we are only interested in the maximum amplitude and frequency range of VIV, RANS is a suitable tool. We have shown that RANS is able to compute the main aerodynamic characteristics in a time saving manner. The improvement of DDES in terms of accuracy is poorly related to its computational cost. When comparing the lock-in regime, RANS tends to a premature synchronisation.For the investigated testcase RANS is conservative in terms of lock-in frequency and maximum amplitude of VIV. The DDES simulation showed some small differences in amplitude at the edge of the lock-in regime, but the main characteristics are still the same. Looking at the unsteady aerodynamics, especially in the wake behind the airfoil, we see some impressive effects on the resolved turbulence. The small-scale eddies computed by DDES disappear when lock-in occurs. This leads to a significant loss of turbulent kinetic energy in the wake behind the airfoil. Thus, the maximum turbulent kinetic energy outside the lock-in regime is about ten times higher than inside. In addition to this effect the spanwise correlation increases. This shows that turbulent flow can be affected by motion. This leads to some interesting ideas related to active flow control. Reducing the turbulent kinetic energy with some moving parts and synchronising the flow in the spanwise direction may cause a significant reduction in noise emissions or may lead to a reduction of drag in turbulent flow.

5 REFERENCES

[1] Williamson, C. and Govardhan, R. (2004). Vortex-induced vibrations. *Annual Review of Fluid Mechanics*, 36(1), 413–455.

[2] Im, H., Chen, X., and Zha, G. (2011). Detached eddy simulation of transonic rotor stall flutter using a fully coupled fluid-structure interaction. *Proceedings of the ASME Turbo Expo*, 6.

[3] Patel, P., Im, H.-S., and Zha, G. (2020). Numerical investigation of non-synchronous vibration with fluid-structure interaction using delayed detached eddy simulation. *AIAA Scitech 2020 Forum*.

[4] Sun, T., Petrie-Repar, P., Vogt, D., et al. (2019). Detached-eddy simulation applied to aeroelastic stability analysis in a last-stage steam turbine blade. *Journal of Turbomachinery*, 141, 1.

[5] Wang, B. and Zha, G.-C. (2011). Detached-eddy simulation of transonic limit cycle oscillations using high order schemes. *Computers Fluids*, 52, 58–68.

[6] Williamson, C. and Roshko, A. (1988). Vortex formation in the wake of an oscillating cylinder. *Journal of Fluids and Structures*, 2(4), 355–381.

[7] Nguyen, V.-T. and Huy, N. (2016). Detached eddy simulations of flow induced vibrations of circular cylinders at high reynolds numbers. *Journal of Fluids and Structures*, 63, 103–119.

[8] Norberg, C. (2003). Fluctuating lift on a circular cylinder: review and new measurements. *Journal of Fluids and Structures*, 17(1), 57–96.

[9] Hover, F., Miller, S., and Triantafyllou, M. (1997). Vortex-induced vibration of marine cables: Experiments using force feedback. *Journal of Fluids and Structures*, 11(3), 307–326.

[10] Skrzypiński, W., Gaunaa, M., Sørensen, N., et al. (2014). Vortex-induced vibrations of a du96-w-180 airfoil at 90° angle of attack. *Wind Energy*, 17(10), 1495–1514.

[11] Zou, F., Riziotis, V. A., Voutsinas, S. G., et al. (2015). Analysis of vortex-induced and stall-induced vibrations at standstill conditions using a free wake aerodynamic code. *Wind Energy*, 18(12), 2145–2169.

[12] Horcas, S. G., Barlas, T., Zahle, F., et al. (2020). Vortex induced vibrations of wind turbine blades: Influence of the tip geometry. *Physics of Fluids*, 32, 065104.

[13] Iyer, S. S. (2023). Unsteady aerodynamics and vortex shedding of a wind turbine blade. master thesis, Technical University of Denmark and Delft University of Technology.

[14] Benner, B. M., Carlson, D. W., Seyed-Aghazadeh, B., et al. (2019). Vortex-induced vibration of symmetric airfoils used in vertical-axis wind turbines. *Journal of Fluids and Structures*, 91, 102577.

[15] Grinderslev, C., Houtin-Mongrolle, F., Nørmark Sørensen, N., et al. (2023). Forced-motion simulations of vortex-induced vibrations of wind turbine blades – a study of sensitivities. *Wind Energy Science*, 8(10), 1625–1638.

[16] Garbaruk, A., Shur, M., Strelets, M., et al. (2009). 3 naca0021 at 60° incidence. In *DESider – A European Effort on Hybrid RANS-LES Modelling*. Berlin, Heidelberg: Springer Berlin Heidelberg. ISBN 978-3-540-92773-0, pp. 127–139.

[17] Spalart, P., Jou, W.-H., Strelets, M., et al. (1997). Comments on the feasibility of les for wings, and on a hybrid rans/les approach. *Advances in DNS/LES: Direct numerical simulation and large eddy simulation*, 137–148.

[18] Spalart, P. (2009). Detached-eddy simulation. *Annual Review of Fluid Mechanics*, 41, 181–202.

[19] Spalart, P. R. and Streett, C. (2001). Young-person's guide to detached-eddy simulation grids. Tech. Rep. NASA/CR-2001-211032, NASA.

[20] Swalwell, K., Sheridan, J., and Melbourne, W. (2003). Frequency analysis of surface pressures on an airfoil after stall. *21st AIAA Applied Aerodynamics Conference*, 1–8.

[21] Nitzsche, J. (2005). Simulation des transsonischen Flatterns eines Tragflügelmodells im Zeitbereich. Master thesis, Technische Fachhochschule Berlin, Berlin.

[22] Zhou, Z., Wen, Y., Cai, C., et al. (2021). Chapter 7 - step-by-step integration method. In *Fundamentals of Structural Dynamics*. Elsevier, pp. 245–266.

[23] Morse, T. and Willamson, C. (2009). Prediction of vortex-induced vibration response by employing controlled motion. *Journal of Fluid Mechanics*, 634, 5 – 39.

COPYRIGHT STATEMENT